Department
of
APPLIED MATHEMATICS

Numerical Methods for Flow in a Porous Media with Internal Boundaries

by

Brit Gunn Ersland and Magne S. Espedal

Report no. 105 February 1997

UNIVERSITY OF BERGEN
Bergen, Norway

Department of Mathematics
University of Bergen
5007 Bergen
Norway

ISSN 0084-778x

Numerical Methods for Flow in a Porous Media with Internal Boundaries

by

Brit Gunn Ersland og Magne S. Espedal

Report No. 105

February 1997

Numerical Methods for Flow in a Porous Media with Internal Boundaries

BRIT GUNN ERSLAND, MAGNE S. ESPEDAL,
Department of Mathematics
University of Bergen
Bergen, Norway

Abstract

Flow of fluids and transport of solutes in porous media are subjects of wide interest in several fields of applications: reservoir engineering, subsurface hydrology, chemical engineering, etc. In this paper we will study a two-phase flow model where the capillary pressure is a function both of saturation and the absolute permeability.

The absolute permeability may be a discontinuous function in space. This lead to interior boundary value problems where the saturation S_w also will be discontinuous. A new solution procedure for such problems will be presented. The method combine the modified method of characteristics with a weak formulation where the basisfunctions are discontinuous at the interior boundary. The modified method of characteristics will provide a good first approximation for the jump in the discontinuous basis functions, which leads to a fast converging iterative solution scheme for the complete problem.

The method has been implemented in a two-dimensional simulator and results from numerical experiments will be presented.

1 Introduction.

A reservoir may consist of several different types of sediments, which in general have different porosity, ϕ, and absolute permeability, $\mathbf{K}$. Therefore, these quantities are functions of the spacial coordinates. In this paper we will develop solution methods for two phase, immiscible flow in such media. We will study a petroleum reservoir model where the phases are water (w) and

oil (o), but the methods presented, may easily be extended to groundwater problems where the phases may be water and air. Let $S = S_w$ denote the water saturation. Then the incompressible displacement of oil by water in the porous media can be described by the following set of partial differential equations:

$$\nabla \cdot \mathbf{u} = q_1(\mathbf{x}, t), \tag{1}$$

$$\mathbf{u} = -\mathbf{K}(\mathbf{x})M(S, \mathbf{x})(\nabla p), \tag{2}$$

$$\phi(\mathbf{x})\frac{\partial S}{\partial t} + \nabla \cdot (f(S)\mathbf{u}) - \varepsilon \nabla \cdot (D(S, \mathbf{x})\nabla S) = q_2(\mathbf{x}, t)\,. \tag{3}$$

Here, $\mathbf{u}$ is the total Darcy velocity, which is the sum of the Darcy velocities of the oil and water phases:

$$\mathbf{u} = \mathbf{u}_o + \mathbf{u}_w\,.$$

Furthermore, $q_1(\mathbf{x}, t)$ denotes injection and production wells, p is the total fluid pressure and $M(S, \mathbf{x})$ denotes the total mobility of the phases:

$$M(S, \mathbf{x}) = \lambda_o(S) + \lambda_w(S)$$

where

$$\lambda_l = \frac{k_{rl}(S)}{\mu_l}\,,\ l = o, w\,.$$

The relative permeabilities, k_{rl} of oil and water, may also be different for diferent sediments, but we will assume that they only are functions of the water saturation S. μ_l is the viscosity of the phases.

Equation (3) is the fractional flow formulation of the massbalance equation for the water saturation. The fractional flow function $f(S)$ is typically a S shaped function of saturation, defined by

$$f(S) = \frac{\lambda_w(S)}{\lambda_w(S) + \lambda_o(S)}\,. \tag{4}$$

The diffusion function is given by:

$$D(S, \mathbf{x}) = K(\mathbf{x})f(S)\lambda_o(S)\frac{\partial P_c}{\partial S}, \tag{5}$$

where $P_c(S, \mathbf{x})$ is the capillary pressure function. ε is a parameter which scales the diffusion term. For a complete survey and justification of the model we refer to [11]. We have neglected gravity forces, but the methods described can also be used for models where gravity effects are included.

2 Model specifications.

The parameters that depend on the porous media are

- $\mathbf{K}(\mathbf{x})$ the absolute permeability,
- k_{ro}, k_{rw} the relative permabilities of oil and water,
- ϕ the porosity of the rock.
- $P_c(S, \mathbf{x})$ the capillary pressure.

In this work the porosity is kept constant; a reasonable choice is $\phi = 0.2$.

We assume that there is only a small number of layers, usually two sediments, with a sharp boundary between them. Variation in relative permeabilities over an interior boundary, where the capillary pressure forces are neglected, is studied in [18, 19, 22]. A more extensive study of such models where capillary forces are included, is given by Ersland [1]. Since several laboratory experiments shows that capillary pressure forces have large effect on displacement of oil by water in a layered porous media [20, 8, 7, 16, 6, 4, 23], we will give the capillary pressure forces major attention and keep the relative permeabilities independent of the faces of the porous media. For our purpose it will be sufficient to consider the following analytical forms:

$$\begin{aligned} k_{rw} &= S^2\,, \\ k_{ro} &= (1-S)^2\,. \end{aligned}$$

The capillary pressure function may depend on the porosity and the permeability of the rock [10, 27]. In this work we use a slightly modified capillary pressure function from the one given in [10, 27]:

$$P_C(S, \mathbf{x}) = 0.9\phi^{-0.9}\mathbf{K}^{-\beta}\frac{1-S}{\sqrt{S}}, \tag{6}$$

where we have chosen $\beta = 0.1$.

In figure 1 the capillary pressure function, and diffusion function are plotted for different permeabilities.

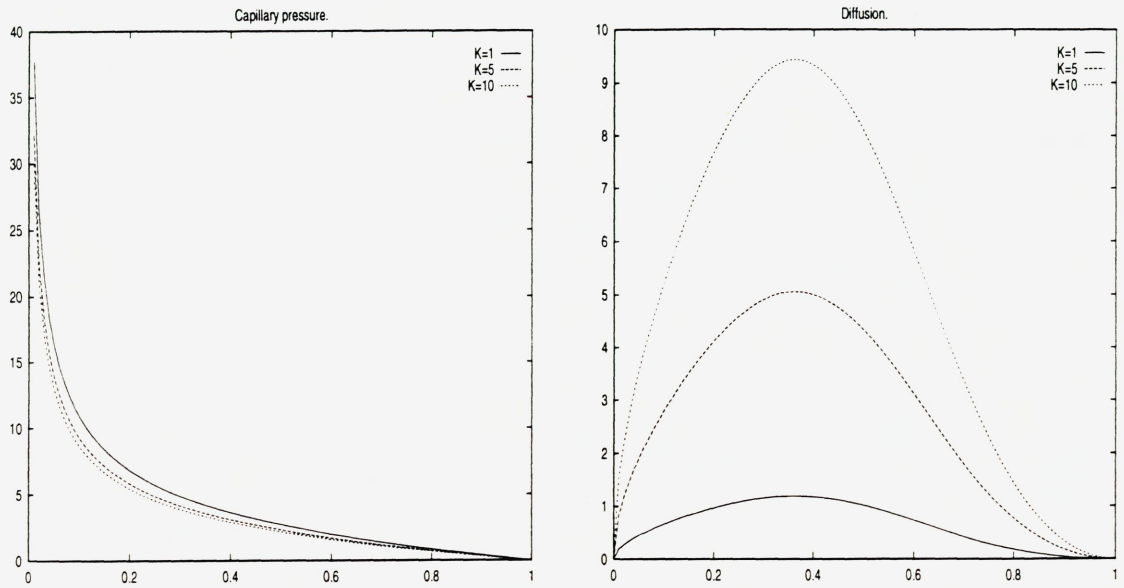

Figure 1: *Capillary pressure and diffusion as functions of saturation for permeability 1, 5 and 10 with* $\beta = 0.1$.

The phase pressures are continuous over interior boundaries, therefor the capillary pressure also is continuous over the interior boundaries. Furthermore, the flux must be continuous over interior boundaries [5, 26] which give the following internal boundary conditions:

$$P_C^{\Gamma-}(S^{\Gamma-}) = P_C^{\Gamma+}(S^{\Gamma+}) \tag{7}$$

and

$$(\mathbf{u}^{\Gamma-} - \mathbf{u}^{\Gamma+}) \cdot \mathbf{n}^{\Gamma} = 0$$

$$(f(S^{\Gamma-})\mathbf{u} - \varepsilon D^{\Gamma-}(S^{\Gamma-}, \mathbf{x})\nabla S^{\Gamma-}) \cdot \mathbf{n}^{\Gamma} = (f(S^{\Gamma+})\mathbf{u} - \varepsilon D^{\Gamma+}(S^{\Gamma+}, \mathbf{x})\nabla S^{\Gamma+}) \cdot \mathbf{n}^{\Gamma}. \tag{8}$$

Here $(\cdot)^{\Gamma-}$ and $(\cdot)^{\Gamma+}$ denote the left and right hand side value at the interior boundary Γ , and $\mathbf{n}^{\Gamma}$ is normal to the boundary.

Since the capillary pressure depends on both the saturation and the permeability, the continuity of the capillary pressure leads to discontinuous saturation over the interior boundary. This adds extra complexity to our problem especially when a saturation front passes it.

2.1 Solution procedure

The governing equations (1) , (2) and (3) are coupled. A sequential, time marching strategy is used to decouple the equations. This strategy reflects the different natures of the elliptic pressure equation given by (1) and (2), and the convection dominated parabolic saturation equation (3) .
The velocity is a smoother function in space and time than the saturation. Therefore we solve the pressure and velocity equations with the saturation at the present time to linearize the nonlinear coefficients of the pressure and velocity equation. Then the new velocity field is used when the saturation is advanced to the next time level by solving equation (3) . In this way different solution strategies and discrete scales can be chosen independently for each of the problems (1) , (2) and (3).

The solution of the pressure and velocity equation is not considered as a main issue in this work.
A combination of equation (1) and (2) gives an elliptic pressure equation with a discontinuous permeability. This equation may be solved in a weak form, using a standard Galerkin method with bilinear elements [2, 28].

Then the velocity is derived from the Darcy equation (2), using local flux conservation over the elements [28]. This gives the same accuracy for the velocity field as for the pressure. The mixed finite element method would be an alternative solution procedure.

To investigate the method we assume that our computational domain consists of two rectangles with a common boundary Γ, see Figure 2.

Water is injected at the left boundary, while oil is produced at the right side of the domain.

3 A basis for discontinuous functions.

In the following section we will study the weak formulation of the parabolic saturation equation (3) and show that a basis can be constructed so that condition (7) is satisfied over the interface between two adjacent sediments. In addition we require that the solution satisfies condition (8). One important feature here is that the jump across the interface is nearly constant in time, except when a saturation front is passing.

Consider a grid on $\Omega = \Omega_1 \bigcup \Omega_2$ depicted in Figure 2, and let the grid

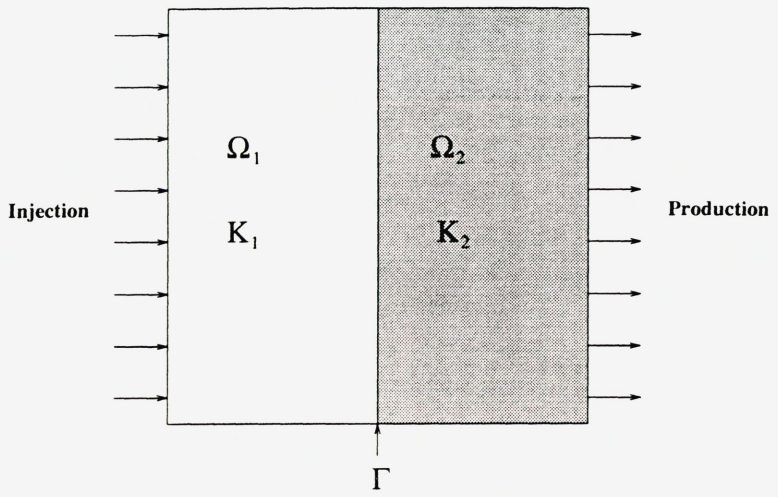

Figure 2: *Computational domain showing two different regions with different physical properties connected through an interior boundary.*

coincide with the interior interface Γ separating the sediments. On each subdomain Ω_1 and Ω_2, the following integral formulation is valid:

$$\int_{\Omega_m} \phi \frac{\partial S}{\partial t} v d\Omega + \int_{\Omega_m} \nabla \cdot (f(S)\mathbf{u} - \epsilon D(S,\mathbf{x})\nabla S) v d\Omega = \int_{\Omega_m} q_2(\mathbf{x},t) d\Omega\,, \quad (9)$$

for all $v \in H^1(\Omega_i)$, $m = 1,2$. By Gauss theorem and by assuming no-flux conditions at the outer boundaries we get the following weak formulations:

$$\begin{aligned} &\int_{\Omega_m} \phi \frac{\partial S}{\partial t} v d\Omega - \int_{\Omega_m} (f(S)\mathbf{u} - \epsilon D(S,\mathbf{x})\nabla S) \cdot \nabla v d\Omega \\ &+ \int_{\Gamma} (f(S)\mathbf{u} - \epsilon D(S,\mathbf{x})\nabla S) v \cdot \mathbf{n}_m d\Gamma = \int_{\Omega_m} q_2(\mathbf{x},t) d\Omega\,, m = 1,2, \end{aligned} \quad (10)$$

where $\mathbf{n}_m$ denotes the outward unit normal to Ω_m so that $\mathbf{n}_1 = -\mathbf{n}_2$ on Γ. Hence, by summing over m and using continuity in flux, we get

$$\sum_{m=1}^{2} \int_{\Omega_m} (\phi \frac{\partial S}{\partial t} v - (f(S)\mathbf{u} - \epsilon D(S,\mathbf{x})\nabla S) \cdot \nabla v) d\Omega = \sum_{m=1}^{2} \int_{\Omega_m} q_2(\mathbf{x},t) d\Omega\,, \quad (11)$$

for all $v \in H^1(\Omega)$.
we may note that $v \in H^1(\Omega) \Rightarrow v|_{\Omega_m} \in H^1(\Omega_m)$.

To simplify the exposition, we restrict the construction of a trial space representing discontinuous functions, to one spatial dimension. However, the method is applicable in more than one spatial dimension, e.g., on bilinear elements (see section 6).

In order to satisfy the interior boundary condition (7) we must allow solutions to be discontinuous across the interface, but continuous elsewhere. To achieve this, let the basis function $\phi_i(x)$ be given by

$$\phi_i(x) = \begin{cases} 0\,, & x < x_{i-1}\,, \\ c_i\theta_i(x)\,, & x_{i-1} \le x \le x_i\,, \\ (2 - c_i)\theta_i(x)\,, & x_i \le x \le x_{i+1}\,, \\ 0\,, & x > x_{i+1}\,, \end{cases} \tag{12}$$

where

$$c_i = 1.0 - \frac{[S]_i}{2\langle S\rangle_i}\,. \tag{13}$$

and $\theta_i(x)$ is the hat function (41).

Here, $[S]_i$ denotes the jump and $\langle S\rangle_i$ the average over a node x_i, i.e.:

$$[S]_i = S(x_i^+) - S(x_i^-) \tag{14}$$

and

$$\langle S\rangle_i = \frac{1}{2}(S(x_i^+) + S(x_i^-))\,. \tag{15}$$

Since $[S]_i = 0$ and $\langle S\rangle_i = S(x_i)$ when $i \neq k$ where $\Gamma = x_k$, this implies that $c_i = 1$ when $i \neq k$, and the expansion

$$S(x) = \sum_i \langle S\rangle_i \phi_i \tag{16}$$

exactly represents the jump $[S]_k$ over x_k. The basis functions are depicted in Figure 3.

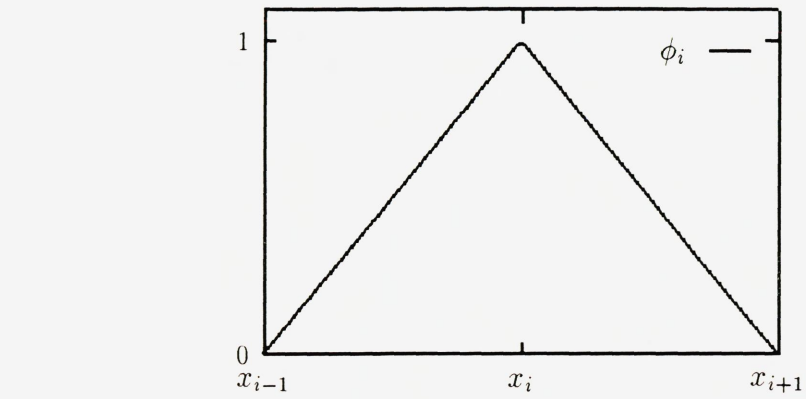

(a)

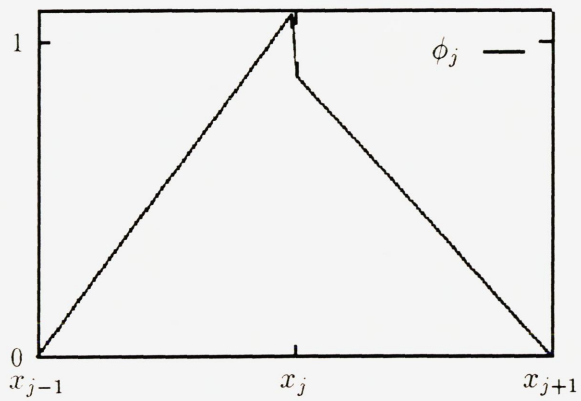

(b)

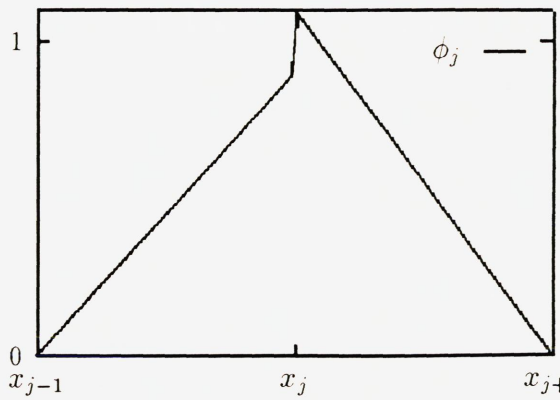

(c)

Figure 3: *Discontinuous basis functions. (a): Basis function when* $k \neq i$ *or when* $S^{\Gamma-} = S^{\Gamma+}$. *(b): Basis function when* $S^{\Gamma-} > S^{\Gamma+}$ *that is* K *on* Ω_1 *is smaller than* K *on* Ω_2. *(c): Basis function when* $S^{\Gamma-} < S^{\Gamma+}$ *that is* K *on* Ω_1 *is larger than* K *on* Ω_2.

Hence the extra degree of freedom required to represent a discontinuity in saturation has now become an explicit part of the trial functions through

c_k, which is determined by condition (7) (continuity of pressure).
It is important to note that in terms of the average saturation $\langle S \rangle$ given by equation 15, the solution procedure is a conformal finite element formulation on the domain Ω. All the coefficients in the representation 16 of the saturation S is determined through the average saturation. The extra degre of freedom at an internal interface, represented by discontinuous trialfunctions, is determined through the constraint (7).
It turns out that this representation of the solution significantly improve the nonlinear iteration procedure. The main reason for this is that the jump in saturation across the interface does not change very much from time-step to time-step, unless a front is passing. Hence, by using the jump at the previous time-level as a start-iterate, a fairly good estimate of condition (7) is already built into the method.

A backward-Euler scheme is used to discretize equation (11) in time. Note that this imposes a CFL-constraint on the time step. The nonlinear coefficients in (11) are linearized by Picard iterations. To be more precise: Let

$$S_p^{n+1} = \sum \langle S \rangle_i^p \phi_i^{p-1}(x) \tag{17}$$

be the p-te approximate solution at time-level t^{n+1} . Here

$$\phi^{p-1}(x) = \begin{cases} 0\,, & x < x_{i-1}\,, \\ c_i^{p-1}\theta_i(x)\,, & x_{i-1} \le x \le x_i\,, \\ (2 - c_i^{p-1})\theta_i(x)\,, & x_i \le x \le x_{i+1}\,, \\ 0\,, & x > x_{i+1}\,, \end{cases} \tag{18}$$

where $c_i^{p-1} = 1 - \frac{[S]_i^{p-1}}{2\langle S \rangle_i^{p-1}}$. Let $S^n(x)$ be the approximation at time level t^n and $V^h(\Omega) = span\,\{\psi_i(x)\} \subset H^1(\Omega)$ be the test-space, given by (40). Then S_p^{n+1} is the solution of

$$\sum_{m=1}^{2} \int_{\Omega_m} (S_p^{n+1} v - \frac{\Delta t}{\phi}(f(S_{p-1}^{n+1}) - \epsilon D(S_{p-1}^{n+1}) \nabla S_p^{n+1}) \cdot \nabla v) d\Omega = \sum_{m=1}^{2} \int_{\Omega_m} (S^n + \frac{\Delta t}{\phi} q_2(x, t^{n+1}) d\Omega \tag{19}$$

for all $v \in V^h(\Omega)$. The jump parameter c_k^{p-1} is determined successively by solving

$$\langle S \rangle_k^{p-1} = \frac{1}{2}(S_k^{(p-1)-} + S_k^{(p-1)+}) \tag{20}$$

and

$$P_{C-}(S_k^{(p-1)-}) = P_{C+}(S_k^{(p-1)+}) \tag{21}$$

by an iteration procedure [1].

If the Picard iteration has converged, the following limits are valid:

$$\lim_{x \to x_k^-} \langle S \rangle_k \phi_k(x) = \lim_{x \to x_k^-} \frac{1}{2}(S^{\Gamma-} + S^{\Gamma+}) c \frac{x - x_{k-1}}{h} = S^{\Gamma-}, \tag{22}$$

and

$$\lim_{x \to x_k^+} \langle S \rangle_k \phi_k(x) = \lim_{x \to x_k^+} \frac{1}{2}(S^{\Gamma-} + S^{\Gamma+})(2 - c) \frac{x_{k+1} - x}{h} = S^{\Gamma+}. \tag{23}$$

In Figure 4 the numerical solution using the discontinuous basis functions, is shown. The solution has been compared with accurate numerical reference solutions [1] and the procedure turns out to be very accurate. Observe that the solution satisfy both the interface conditions (8) and (7).

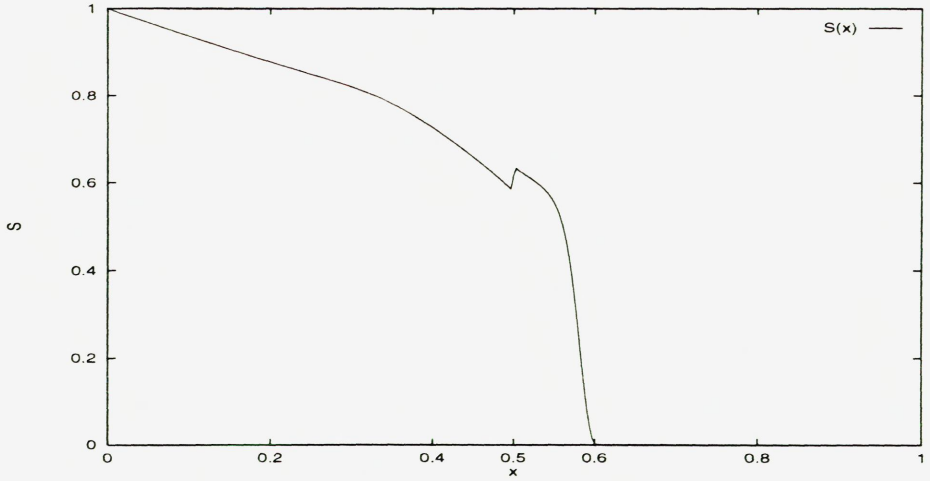

Figure 4: *The saturation profile for a heterogeneous porous medium with permeability* $K = 10.$ *when* $x < 0.5$ *and* $K = 1.$ *when* $x > 0.5$. *The timestep* $\Delta t = 0.0005$, $\Delta x = 1/300$, *and* $\epsilon = 0.01$. *at* $t = 0.024$, *the discontinuous basis is used.*

4 Operator splitting with a discontinuous basis.

The normal backward-Euler scheme used in the previous section, require very small timesteps. Therefore, we will extend an operator splitting technique with backward integration along characteristics to the interface problem given above. This method has been shown to work well for large time steps [17, 12, 13].

We will combine the modified method of characteristics with the discontinuous basis which was introduced in previous section. This approach will provide a better first guess for the discontinuous basis functions than the solution at previous time step, especially when the saturation front is passing the interface. Hence, the number of picard iterations which are needed for the method to converge will decrease.

The parabolic saturation equation (3) is dominated by the convective

part for large flow-rates $\mathbf{u}$. This is the typical scenario in oil recovery, though in the vicinity of sharp fronts and close to interior boundaries capillary forces play important roles.

Therefore, we will use a two step splitting procedure [17, 14, 12] in the solution of equation (3).

In the first step a modified convective time derivative is calculated:

$$(\psi(\mathbf{x})\frac{\partial S}{\partial \tau}) \equiv (\phi\frac{\partial S}{\partial t} + \nabla \cdot (\bar{f}(S)\mathbf{u}) = 0 \tag{24}$$

where the fractional flow function $f(S)$ has been splitted in two parts:

$$f(S) = \bar{f}(S) + b(S)S\,, \tag{25}$$

where $\bar{f}(S)$ is a convex or concave envelope of the fractional flow function $f(S)$, depending on the sign of $(\mathbf{u} \cdot \nabla S)$ [15] and gives the unique physical velocity of an established shock.
Then, the solution of (24) is used iteratively to approximate the characteristic derivative and the nonlinear coefficients in equation (3):

$$(\psi(\mathbf{x})\frac{\partial S}{\partial \tau} + \nabla \cdot (b(S)S\mathbf{u} - \epsilon D(S)\nabla S) = 0 \tag{26}$$

Equation (26) is solved in a weak form, using optimal test functions [3, 21, 12] (see Apendix).

On each subdomain Ω_1 and Ω_2 the integral formulation in (9) is valid. With the operator splitting technique described above [17, 13], we get the following form of equation (9):

$$\int_{\Omega_m} \phi\frac{\partial S}{\partial t} v d\Omega + \int_{\Omega_m} \nabla \cdot ((\bar{f}(S) + b(S)S)\mathbf{u} - \varepsilon D(S)\nabla S) v d\Omega = \int_{\Omega_m} q_2(\mathbf{x}, t) v d\Omega\,, \tag{27}$$

where $m = 1, 2$.
To obtain as optimal approximation properties as possible, we will use the Hemker type of test functions v [3, 21, 12, 29]. We rearrange the equations so that the first part denote the major part of the transport, i.e.:

$$\int_{\Omega_m} (\phi\frac{\partial S}{\partial t} + \nabla \cdot (\bar{f}(S)\mathbf{u})) v d\Omega + \int_{\Omega_m} \nabla \cdot (b(S)S\mathbf{u} - \varepsilon D(S)\nabla S) v d\Omega = \int_{\Omega_m} q_2(\mathbf{x}, t) v d\Omega\,, \tag{28}$$

where $m = 1, 2$. Gauss theorem applied on the diffusion correction term gives:

$$\int_{\Omega_m} (\phi \frac{\partial S}{\partial t} + \nabla \cdot (\bar{f}(S)\mathbf{u}))v d\Omega + \int_{\Omega_m} (\varepsilon D(S)\nabla S - b(S)S\mathbf{u}) \cdot \nabla v d\Omega$$
$$+ \int_{\Gamma} (b(S)S\mathbf{u} - \varepsilon D(S)\nabla S)v \cdot \mathbf{n}_m d\Gamma = \int_{\Omega_m} q_2(\mathbf{x}, t) d\Omega\,, \quad m = 1, 2\,, \tag{29}$$

where $\mathbf{n}_m$ is the outward normal to Ω_m. Hence, $\mathbf{n}_1 = -\mathbf{n}_2$ on Γ.
By summing equation (29) over m and using the flux condition (8) we get:

$$\sum_{m=1}^{2} \int_{\Omega_m} (\phi \frac{\partial S}{\partial t} + \nabla \cdot (\bar{f}(S)\mathbf{u}))v d\Omega + \sum_{m=1}^{2} \int_{\Omega_m} (\varepsilon D(S)\nabla S - b(S)S\mathbf{u}) \cdot \nabla v d\Omega$$
$$- \sum_{m=1}^{2} \int_{\Gamma} (\bar{f}(S)v \cdot \mathbf{n}_m d\Gamma = \sum_{m=1}^{2} \int_{\Omega_m} q_2(\mathbf{x}, t) d\Omega\,, \tag{30}$$

since $b(S)S = f(S) - \bar{f}(S)$.
Let

$$\sum_{m=1}^{2} \int_{\Omega_m} (\psi(\mathbf{x}) \frac{\partial S}{\partial \tau})v d\Omega \equiv \sum_{m=1}^{2} \int_{\Omega_m} (\phi \frac{\partial S}{\partial t} + \nabla \cdot (\bar{f}(S)\mathbf{u}))v d\Omega - \sum_{m=1}^{2} \int_{\Gamma} (\bar{f}(S)v \cdot \mathbf{n}_m d\Gamma\,. \tag{31}$$

We apply Gauss theorem on parts of the equation and get

$$\sum_{m=1}^{2} \int_{\Omega_m} (\psi(\mathbf{x}) \frac{\partial S}{\partial \tau})v d\Omega \equiv \sum_{m=1}^{2} \int_{\Omega_m} (\phi \frac{\partial S}{\partial t} - (\bar{f}(S)\mathbf{u}) \cdot \nabla)v d\Omega$$
$$+ \sum_{m=1}^{2} \int_{\Gamma} (\bar{f}(S)v \cdot \mathbf{n}_m d\Gamma - \sum_{m=1}^{2} \int_{\Gamma} (\bar{f}(S)v \cdot \mathbf{n}_m d\Gamma = \sum_{m=1}^{2} \int_{\Omega} (\phi \frac{\partial S}{\partial t} - (\bar{f}(S)\mathbf{u}) \cdot \nabla)v d\Omega\,. \tag{32}$$

To simplify the exposition, we will continue from here in one space dimension. Here as in the previous section the method is applicable in more than one space dimension, see section 5 and 6. Furthermore, we assume that the injection and production wells are given as boundary conditions at the inlet and outlet end.

We recall that the saturation is given by the expansion

$$S(x) = \sum_{i=1} \langle S \rangle_i \phi_i(x) \tag{33}$$

where $\phi_i(x)$ is defined by (12) and $\langle S \rangle_i$ is the average saturation in x_i given by (15). Let $\bar{x}_i$ and $\langle \bar{S} \rangle_i$ be the solution of the nonlinear equations

$$\bar{x}_i = x_i - \bar{f}(\langle S^{n-1} \rangle_i)\Delta t\,, \tag{34}$$

$$\langle S \rangle_i = \sum_i \langle S \rangle_i \theta_i(\bar{x}_i)\,. \tag{35}$$

Now, we use the fact that the averaged saturation $\langle S \rangle$ is continuous, hence:

$$\psi \frac{\partial S^n}{\partial \tau} \approx \phi \frac{S^n - \bar{S}}{\Delta t}\,. \tag{36}$$

Putting this approximation into (30) gives:

$$\sum_{m=1}^{2} \left(\int_{\Omega_m} S^n v d\Omega + \frac{\Delta t}{\phi} \int_{\Omega_m} (\epsilon D(S,x) \frac{\partial}{\partial x} S^n - b(S) S^n) \frac{\partial}{\partial x} v d\Omega \right) = \sum_{m=1}^{2} \int_{\Omega_m} \bar{S} v d\Omega\,. \tag{37}$$

This equation is solved with the discontinuous basis functions defined in (12) in section 3. We use Picard iterations to linearize the nonlinear coefficients, with $\bar{S}$ as a start-iterate and determine the coefficients for the discontinuous basis from $\langle \bar{S} \rangle_i$ and the condition given in (7).

5 Numerical experiments.

A coreplug is a sample of sediments obtained from wellbore cores. In this chapter we will present results for a coreplug and for a rectangular domain where water is injected along one side and oil is produced at the opposite side as given in Figure 2. Let Ω denote the region in space occupied by the coreplug or the rectangular region. The region consists of two different sediments with a sharp boundary between the sediments, see Figure 2. We have named the first sediment Ω_1 , the second Ω_2 and the interface Γ . Hence $\Omega = \Omega_1 \cup \Omega_2 \cup \Gamma$.

Parameter	value	Decription
Δt	0.001	time step
t	[0,048]	time interval
Δx	1/150	mesh size
x	[0,1.0]	computational domain
Γ	0.5	location of interior interface
ϵ	0.01	epsilon the diffusion parameter
μ_o, μ_w	1.0 1.0	viscosity of oil and water
ϕ	0.2	the porosity of the matrix
α_o	2	$k_r o(S) = (1-S)^{\alpha_o}$
α_w	2	$k_{rw}(S) = S^{\alpha_w}$
β	0.1	parameter in the capillary pressure function
iterations	100	maximum number of iterations
tol	0.0001	tolerance for convergence of bisection
precision	0.001	tolerance for convergence of iteration

Table 1: *The input data used in both domains for the test cases.*

Our computational domain Ω is scaled with respect to the size of the coreplug in 1d and with respect to the size of the rectangular domain in 2d. Therefore, $\Omega = [0,1]$ in one space dimension and $\Omega = [0,1] \times [0,1]$ in our 2d tests. All the test cases that are presented in this chapter will have an interior boundary Γ, at $x = 0.5$. We regard both Ω_1 and Ω_2 as homogeneous domains, where the saturation front can be traced using characteristics, (24).

In [1] the results obtained with the discontinuous basis is more extensively studied and compared to the results obtained with a massbalance iteration. The agreement between the two methods is very good.

Further, the discontinuous basis is tested for different permeabilities, different functional dependence on permeability in the capillary pressure function and variation in the injection/production rates.

The input data which are used in the computational examples, are given in tables 1 and 2.

The main issue for this presentation is to demonstrate the effects of the capillary pressure forces on the saturation front as the front crosses an interior boundary. We observe that different permeability fields, as given in table 2

case:	$K(\Omega_1)$	$K(\Omega_2)$
b.	1.0	10.0
c.	10.0	1.0

Table 2: *The permeability fields defining test case a,b and c.*

produce different capillary pressure functions, as defined by (7).

Furthermore, in Figure 1 we observe that for a fixed saturation the capillary pressure is higher in a low-permeable sediment than in a high-permeable sediment. Since $\beta = 0.1$ in the numerical experiments shown in this section, the permeability has large impact on the diffusion function, see Figure 1.

To simplify the computations somewhat, the following initial condition is used in all the 1d experiments:

$$S_0(x) = \begin{cases} 1 - \frac{0.3}{0.4}x\,, & x \leq 0.4 \\ 0\,, & x > 0.4 \end{cases} \tag{38}$$

This represents an established front, located away from the inflow boundary.

In section 3 and 4 we introduced two solution strategies where a discontinuous basis is used to capture the jump in saturation over a interface between two sediments. The first solution strategy uses the discontinuity at previous time step as a first approximation to calculate the basis function at the new time step, while the second method obtain the first approximation by integrating backward along the characteristics of the mean saturation in every grid point.

Figure 5 (a) shows computed solutions where the method in section 3 is used, while the method in 4 is used to comuper the solutions in Figure 5 (b). Here the solution with no Picard iterations (single solve) and 4 Picard iterations is compared. The results for test case c in table 2 are given at the time levels $t = 0.024$ and $t = 0.048$. With the method in section 3 there are some differences between the solution with no Picard iterations and with 4 iterations, especially close to the interior boundary, when $t = 0.024$. When $t = 0.048$ the effect of the Picard iterations is smaller at the boundary, but the error we introduced by using a single solve when the saturation front passed the boundary is transported into Ω_2. The computed solutions with

the method in section 3 is overlapping each other. Hence, the first approximation that we obtain by integrationg backward along the characteristics of the mean saturation i an optimal choise. Furthermore, the method decribed in 3 also requires small timesteps compared to the operatorsplitting method described in section 4.

Computed result with the discontinuous trial functions is compared to the computed results with the discontinuous trial functions combined with backward integration is compared in Figure 6. Both test case b and test case c in table 2 are shown for the time levels $t = 0.024$ and $t = 0.048$, and for both methods 4 Picard iterations are used. We find that there is good agreement between the two methods, they provide approximatly the same results for both test cases.

Picard iterations are expensive to compute in more than one space dimension. Since the method with the backward integration requires no Picard iterations for the test cases shown in this section, this method will be further explored in two spatial dimensions, see section 6.

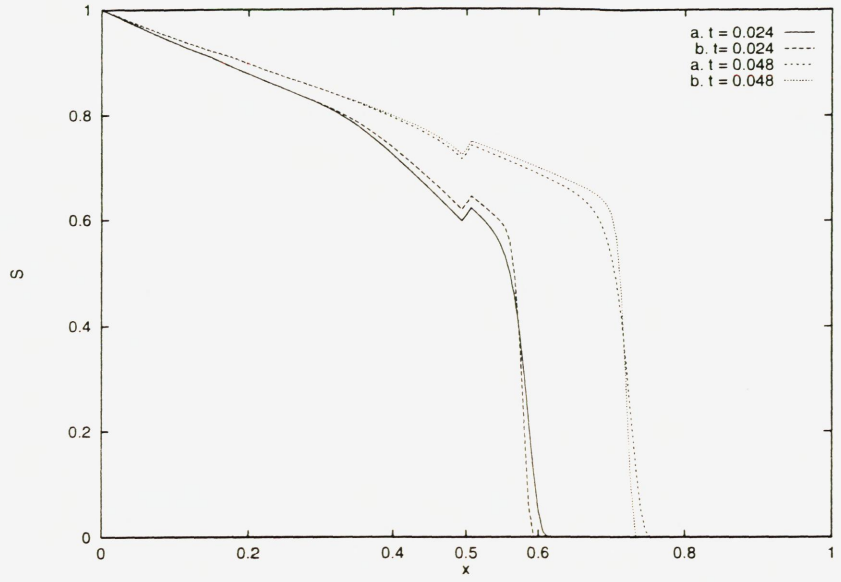

(a) $K(\Omega_1) > K(\Omega_2)$ *(test case c)*

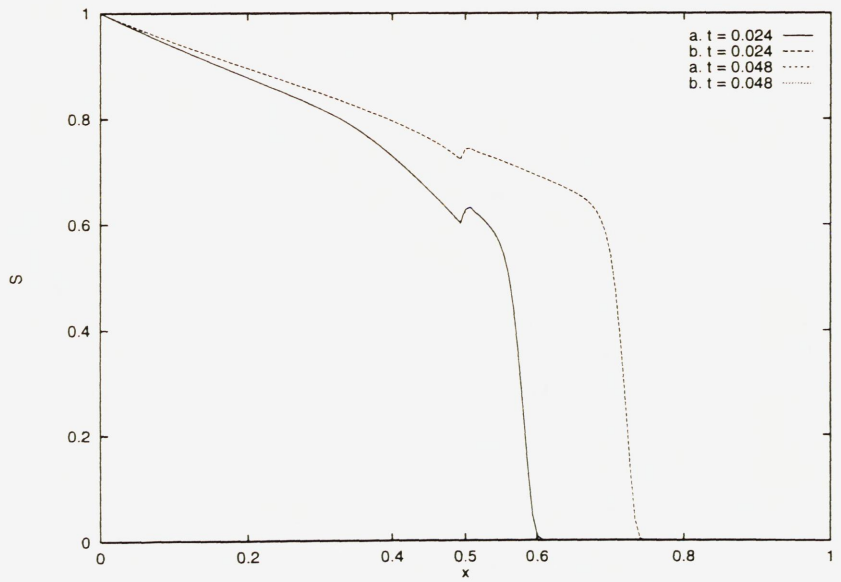

(b) $K(\Omega_1) > K(\Omega_2)$ *(test case c)*

Figure 5: *The saturation profile at time levels* $t = 0.024$ *and* $t = 0.048$ *The solution procedures given in sections 3 and 4 are used for the computations shown in 5(a) and 5(b), respectively.*
a. computation with 4 Picard iterations
b. computation with no Picard iteration (a single solve).
Input data is given in table 1 and 2

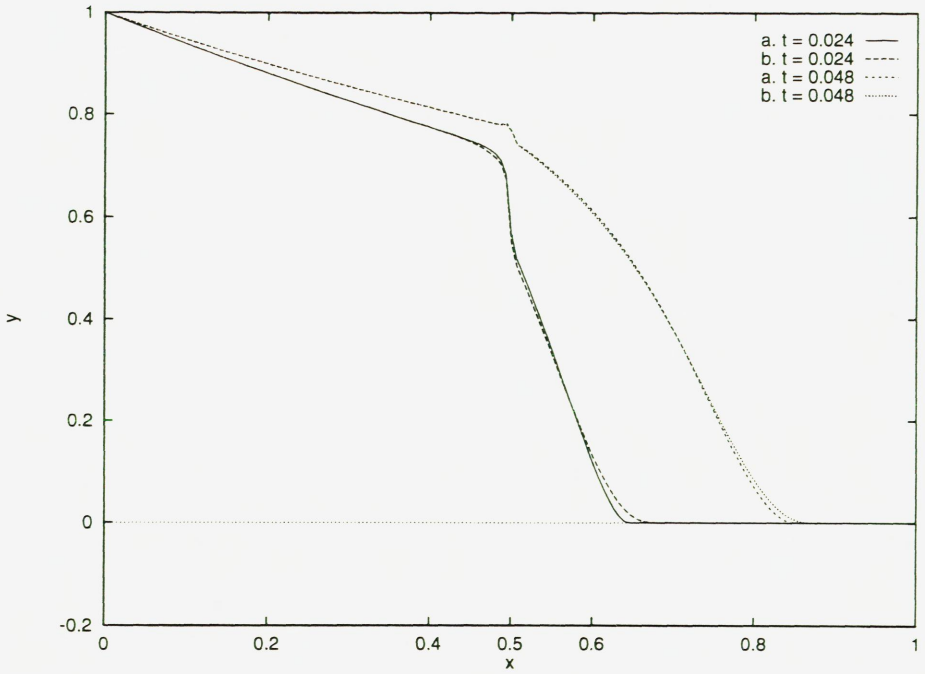

(a) $K(\Omega_1) < K(\Omega_2)$ *test case b.*

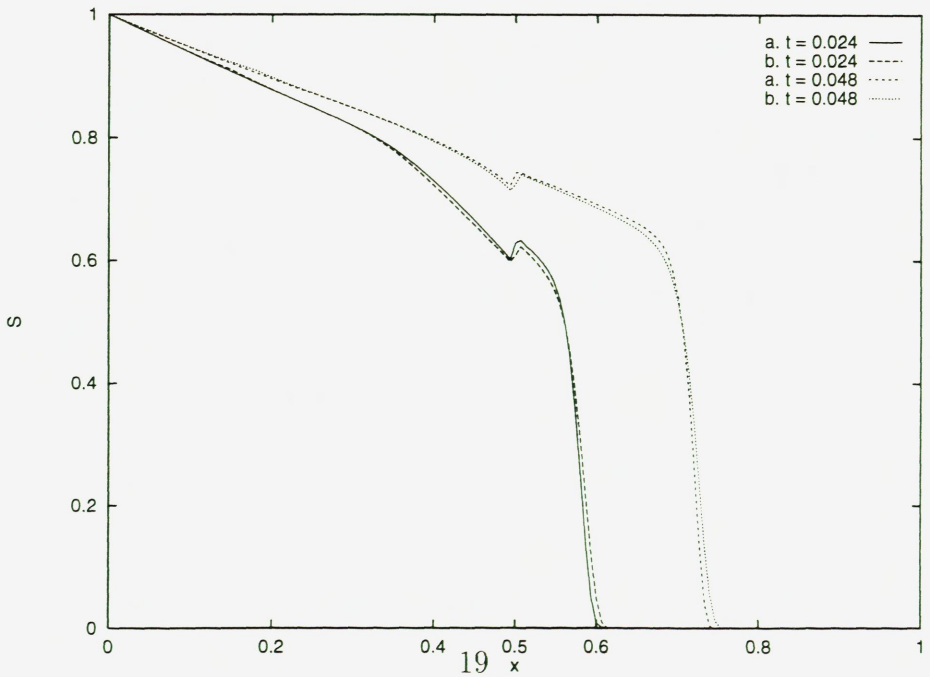

(b) $K(\Omega_1) > K(\Omega_2)$ *test case c.*

Figure 6: *The saturation profile at time level* $t = 0.024$ *and* $t = 0.048$ *. The solution procedure given in section 3 is compared to the solution procedure with backward integration given in section 4 with 4 Picard iterations.*
a. denotes the solution procedure in section 4.
b. denotes the solution procedure in section 3.
Input data is given in table 1 and 2.

6 Numerical results for the five spot problem.

In this part we consider a rectangular domain Ω which is scaled and composed as in section 5. We will have an interior boundary Γ, at $x = 0.5$, and regard both Ω_1 and Ω_2 as homogeneous domains.

A problem with an injector well in lower left corner and a production well in upper right corner, as depicted in Figure 7 are considered.

In this section we will show numerical results computed with the method introduced in 4. Here, the results are computed on a uniform global mesh. However, results obtained with a uniform global mesh are compared to results obtained with adaptive local grid refinement at the front and a fixed local refinement at the interior boundary in [1, 25, 24]. The agreement between the two approaches are good.

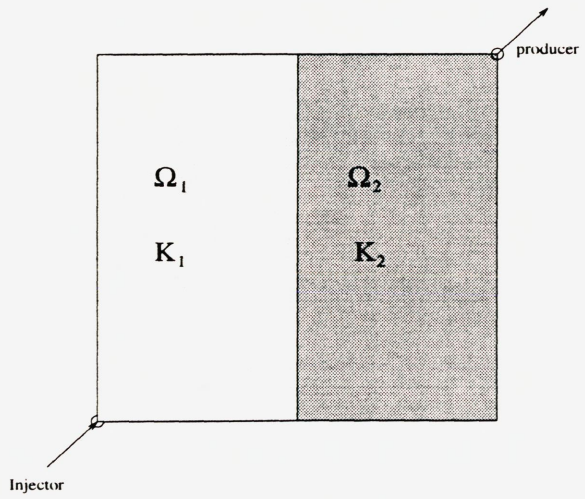

Figure 7: *The computational domain* Ω.

In this section we will present computed results for the five spot problem depicted in Figure 7. Computed saturations for the test cases in table 4 with $\beta = 0.1$, will be shown at four time levels, $t = 0.12$, $t = 0.24$, $t = 0.36$, and $t = 0.48$. Input data which are used in both test cases are given in table 1,

Parameter	value	Decription
dt	0.001	time step
t	[0,36]	time intervall
inj_ rate	0.2	injection rate
prod_ rate	-0.2	production rate

Table 3: *Time and well data for the test cases.*

case:	$K(\Omega_1)$	$K(\Omega_2)$
a	0.1	1.0
b	1.0	0.1

Table 4: *The permeability fields defining test cases a and b. Note that* $\mathbf{K}$ *is a tensor, here* $K_{xx} = K_{yy} = K(\Omega_m)$, $m = 1, 2$ *while* $K_{xy} = K_{yx} = 0$.

while the injection and production rates are given in table 3 together with the time parameters. We use the same linear solvers to compute our results in this section as in section 5.

To simplify the computations somewhat, the following initial condition is used:

$$S_0(x,y) = \begin{cases} 1 - \frac{0.3}{0.4}\sqrt{x^2+y^2}\,, & \sqrt{x^2+y^2} \leq 0.4\,, \\ 0\,, & \sqrt{x^2+y^2} > 0.4\,. \end{cases} \tag{39}$$

This represents an established front, located away from the injection well.

Figure 8 computed saturations for test case a in table 4. Here water is injected in a low permeable sediment, and oil is produced in a high permeable sediment.

The total Darcy velocity and the capillary diffusion depend on the permeability field $\mathbf{K}$,. The effects of different permeabilities and capillary forces in the two regions Ω_1 and Ω_2 combined with the effect of the boundary conditions 7, 8, are clearly seen in Figure 8 (a) - (d). The saturation jump at the internal boundary is negative in this case which means that the displacing fluid is "trapped" at the internal boundary. This effect is to a large degre overcome by the high permeability/diffusion effects in region Ω_2.

A similar problem as the one shown in Figure 8 is treated in [9], where

$K(\Omega_1) = 0.005$ and $K(\Omega_2) = 0.1$. Since the difference between the permeability fields on Ω_1 and Ω_2 is larger in their work than in our test case, the saturation jump at the boundary will be bigger than in the case shown in Figure 8. A Riemann type of simulator is used to track the saturation front. In [9] the capillary pressure forces are neglected, which gives a smooth transition between the two regions.

Except for the internal boundary effects, our result is very similar to the results given in this paper. The results which are obtained with front-tracking method are compared to results obtained with the commercial simulator ECLIPSE. It is shown that the front-tracking method gives "break trough" at a later time level than ECLIPSE. The internal boundary effect will enhance this difference between the simulators.

From Figure 8 we can see that the capillary pressure forces have great impact on the solution close to the boundary between the high and low permeable region.

In Figure 9 computed results for test case b in table 4 are shown. Here the permeability is larger on Ω_1 than on Ω_2, and more of the oil is displaced on Ω_1 than on Ω_2. Along the interface between the high permeable and low permeable region the low permeable matrix acts as a blotting paper. Water is sucked into the low permeable region due to the capillary pressure forces.

We observe in both test cases that the saturation front is more smeared in the high permeable region than in the low permeable region, due to the difference in diffusion.

Finally the computed results show that the method described in section 4 is applicable in a more general case than for one dimensional flow.

The results shown in sections 5 and 6 are computed both with uniform grids and with local refinement based on domain decomposition [1]. The grid is adaptivly refined at the saturation fronts [13, 1] and at the internal boundary. Except for small interpolation effects at the boundary between the coarse and the refined meshes, the results are similar. The domain decomposition version of the code is well suited for parallel computing and also allows us to extend the method to larger scale models.

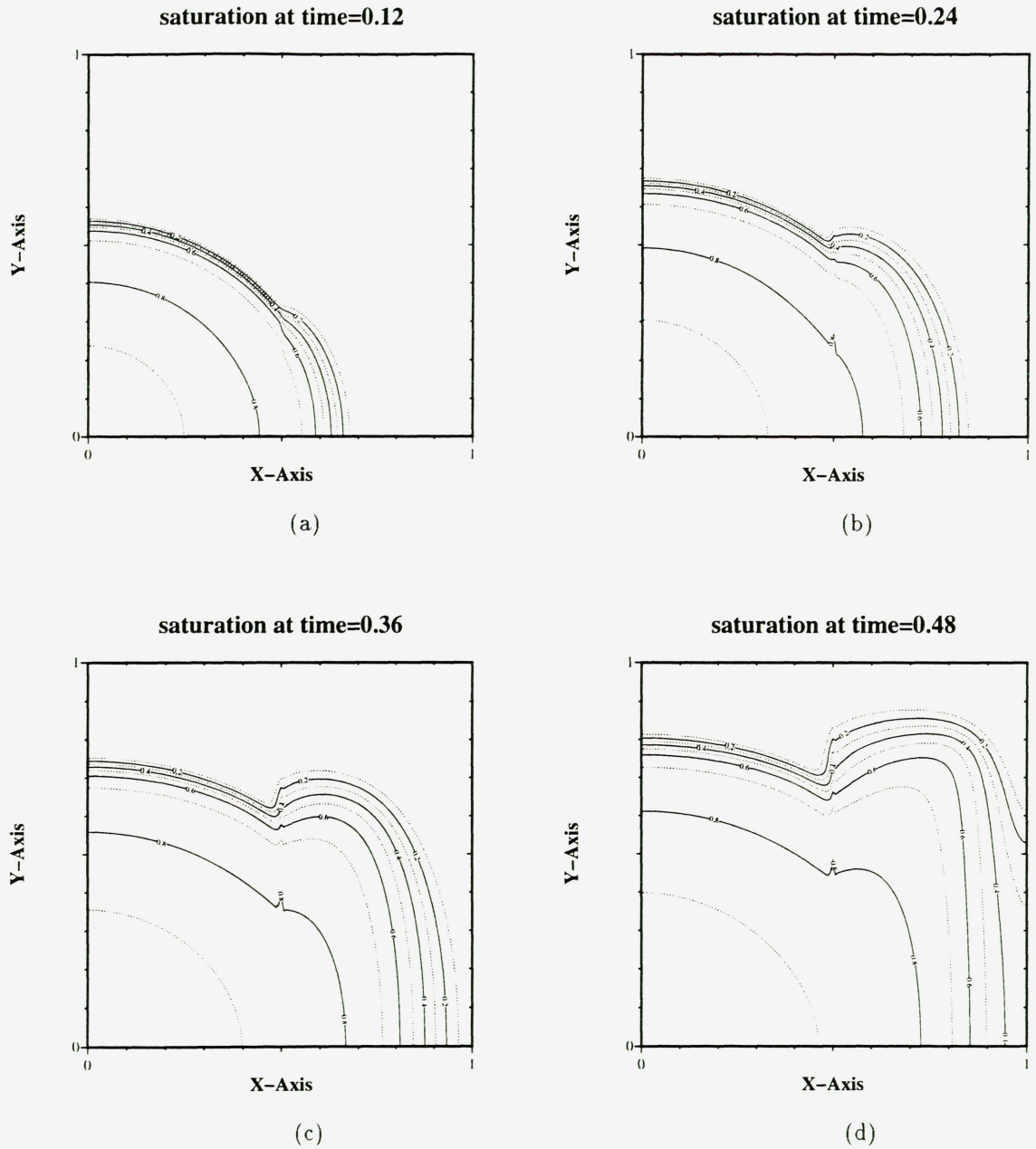

Figure 8: *Saturation profile for five spot problem at time levels* $t = 0.12$, $t = 0.24$, $t = 0.36$ *and* $t = 0.48$. $K(\Omega_1) = 0.1$ *and* $K(\Omega_2) = 1$. *Input data is given in table 1, 3 and 4.*

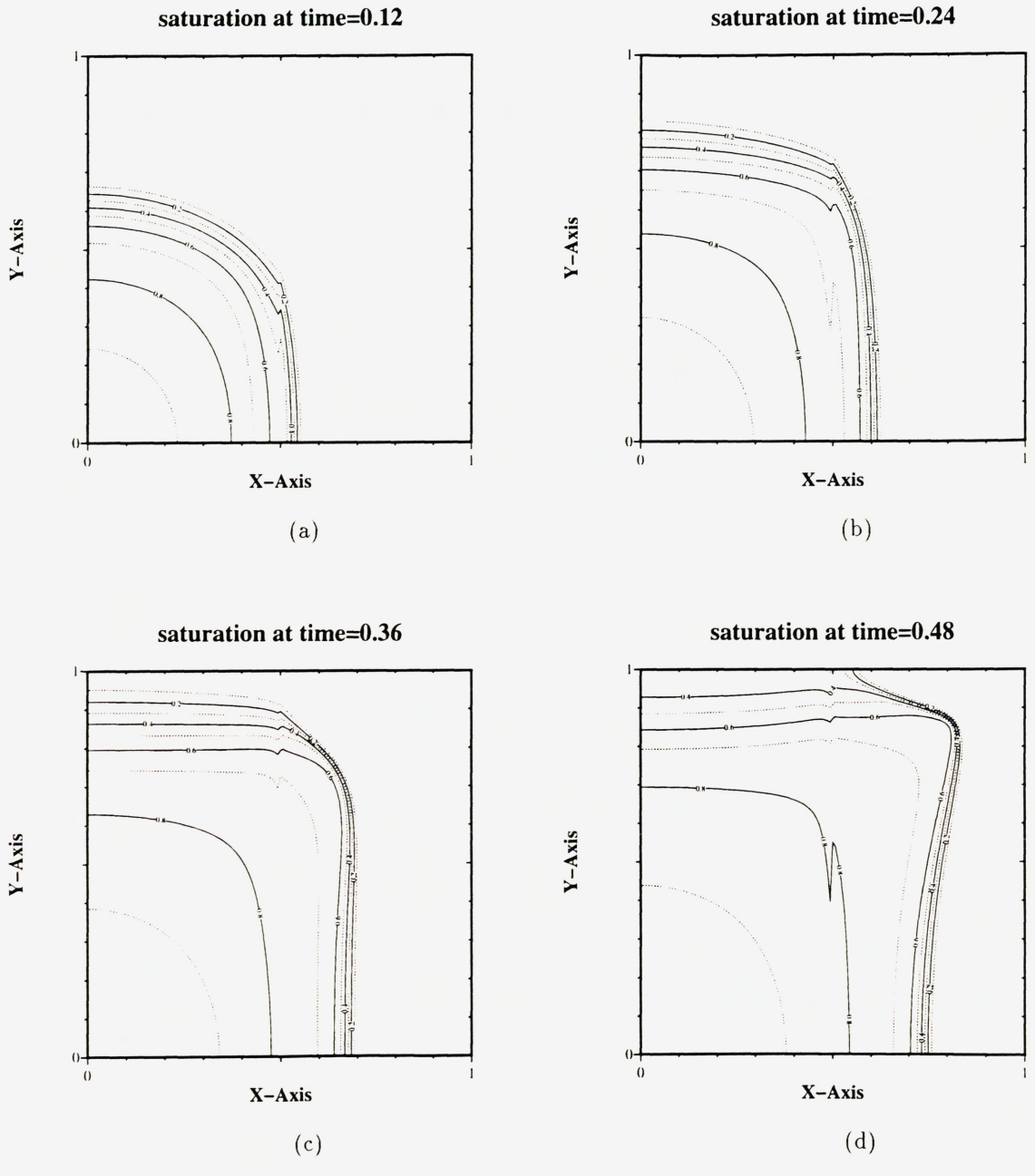

Figure 9: *Saturation profile for five spot problem at time levels* $t = 0.12$, $t = 0.24$, $t = 0.36$ *and* $t = 0.48$. $K(\Omega_1) = 1$ *and* $K(\Omega_2) = 0.1$. *Input data is given in table 1, 3 and 4.*

Acknowledgement

Support from The Norwegian Research Council under the program PROPETRO and by VISTA, a research cooperation between the Norwegian Academy of Science and Letters and Statoil, is gratefully acknowledged.

7 Conclusion

In this work we have focused on solution techniques for the saturation equation for models where the the capillary pressure is a function both of saturation and the absolute permeability. This will be the case if the porous medium consists of layers with different physical properties. Such models lead to discontinuous solutions for the saturation and it is shown that a weak formulation with discontinuous trialfunctions leads to a fast and accurate solution technique. The solution techniques are well suited for local gridrefinement based on domain decomposition. Work is under way to extend the methods to models where also porosity and relative permeability have different functional representation in different parts of a reservoir model.

Appendix

7.1 The test space

As test space we choose a subspace of $H_0^1(\Omega)$. Since the parabolic saturation equation (26) multiplied by the test space and integrated over our computational domain defines a bilinear form we choose the test space so that the bilinear form is approximately symmetrized. The approximation to the solution is near optimal when measured in the norm [3, 21]. In a single space dimension the test functions are defined by:

$$\psi_i(x) = \begin{cases} 0, & x < x_{i-1} \\ \theta_i(x) + c_{i-1}\sigma_i(x), & x_{i-1} \leq x \leq x_i \\ \theta_i(x) + c_i\sigma_i(x), & x_i < x \leq x_{i+1} \\ 0, & x > x_{i+1} \end{cases} . \tag{40}$$

Here, $\theta_i(x)$ is the hat function defined by

$$\theta_i(x) = \begin{cases} 0\,, & x < x_{i-1} \\ \dfrac{x - x_{i-1}}{h}\,, & x_{i-1} \le x \le x_i \\ \dfrac{x_{i+1} - x}{h}\,, & x_i < x \le x_{i+1} \\ 0\,, & x > x_{i+1} \end{cases} \tag{41}$$

and

$$\sigma_i(x) = \begin{cases} \dfrac{(x - x_{i-1})(x - x_i)}{h^2}\,, & x_{i-1} \le x \le x_i \\ -\dfrac{(x - x_i)(x - x_{i+1})}{h^2}\,, & x_i < x \le x_{i+1}\,, \end{cases} \tag{42}$$

is a quadratic perturbation.

$$c_i = 3\left(\frac{2}{\beta_i} - \coth\left(\frac{\beta_i}{2}\right)\right)\,, \qquad \beta_i = \frac{\bar{f}_i h}{\varepsilon \bar{a}_i} \tag{43}$$

where $\bar{f}_i$ and $\bar{a}_i$ denotes $f(S)$ and the diffusion term computed for the saturation at the midpoint of an element i. $f(S)$ is defined by (4) while the diffusion term is given by (5) and h is the parameter of partition. The test functions is depicted in Figure 7.1 for $S > S_f$ in (b), for $0 < S < S_f$ in (c) and for $S = 0$ in (d).

The test functions in 2d is defined by:

$$\psi_{i,j}(x, y) = \psi_i(x)\psi_j(y)\,, \tag{44}$$

where $\psi_i(x)$ and $\psi_j(y)$ is defined above.

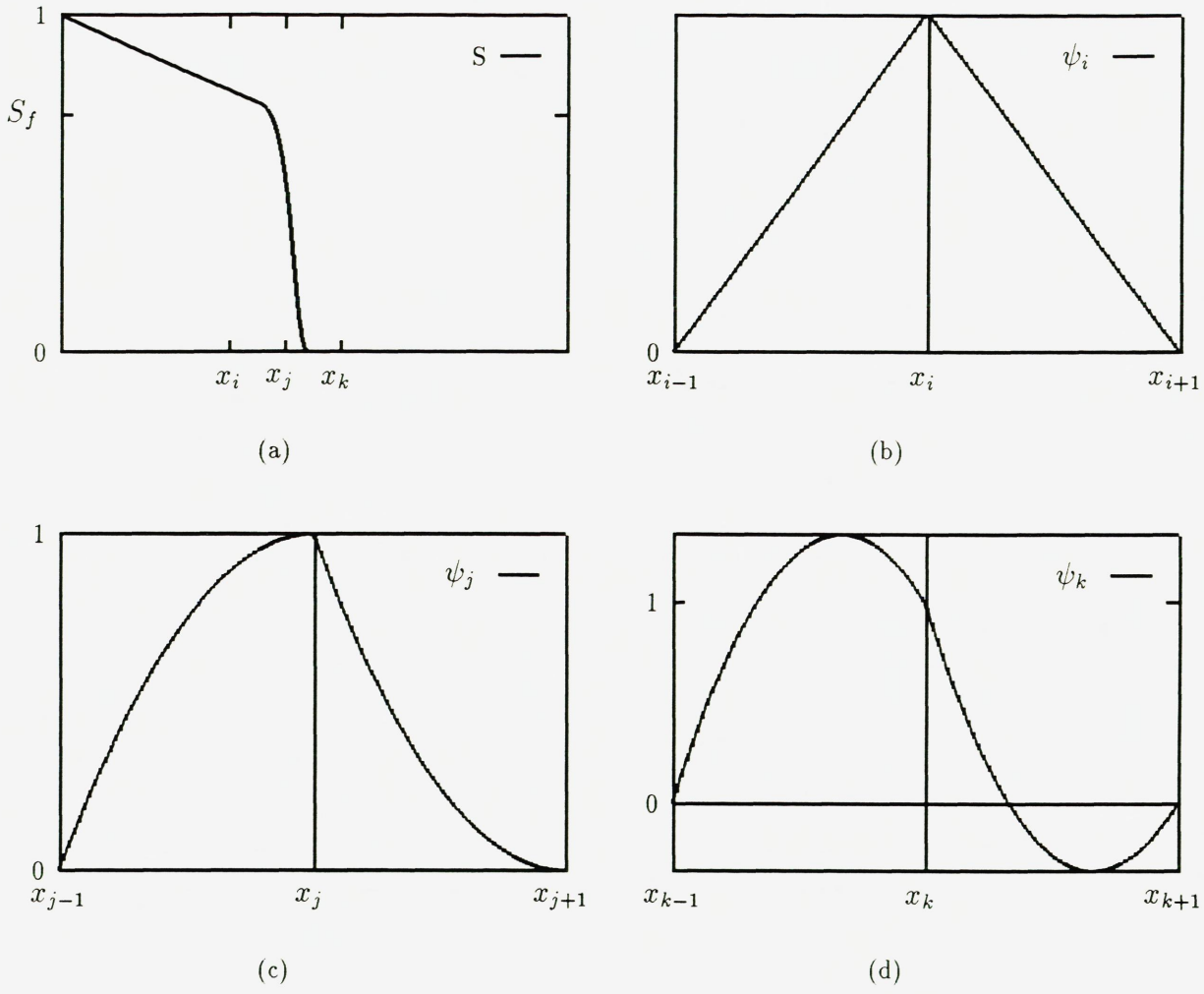

Figure 10: *Typical test functions. (a): One dimensional saturation profile where a point above the shock saturation, a point in the shock region and a point where $S = 0$ is marked. The corresponding test functions is shown in (b), (c) and (d).*
(b): Test function for $S > S_f$. (c): Test function for $S = 1/2S_f$. (d) Test function for $S = 0$.

References

[1] B. G. Ersland. *On Numerical Methods for Including the Effect of Capillary Presure Forces on Two-Phase, Immmiscible Flow in a Layered Porous Media.* PhD thesis, University of Bergen, 1996. Department of Applied Mathematics, University of Bergen.

[2] O. Axelsson and V.A. Barker. *Finite element solution of boundary value problems.* Academic Press, INC., London, England, 1984.

[3] J.W. Barrett and K.W. Morton. Approximate symmetrization and petrov-galerkin methods for diffusion-convection problems. *Computer Methods in Applied Mechanics and Engineering*, 45:97–122, 1984.

[4] H. Bertin, A. Graue, and T. Eilertsen. Two dimensional imaging of viscous and capillary effects in a dipping stratified heterogeneous media. Stavanger, Norway, 1994. International Symposium of the Society of Core Analysts.

[5] Ø. Bøe. *Finete-Element Methods for Porous Media Flow.* PhD thesis, University of Bergen, 1990. Department of Applied Mathematics, University of Bergen.

[6] K.A. Børresen and A. Graue. Fluid flow across capillary heterogeneities, experiments and simulations. submitted to Transport in Porous Media.

[7] K.A. Børresen and A. Graue. Comparing simulations to 2d imaging experiments of fluid flow in a dipping crossbedded reservoir model. In *71th Annual Technical Conference and Exhibition of SPE*, number SPE 36731, Oct. 1996.

[8] K.A. Børresen and A. Graue. Numerical simulations and 2d-imaging experiments of flow in tilted cross beds. In *SCA-symposium*, Sept. 1996.

[9] F. Bratvedt, K. Bratvedt, C.F. Buchholz, L. Holden, H. Holden, and N.H. Risebro. A new front-tracking method for reservoir simulation. *SPE Reservoir Engineering*, pages 107–116, February 1992.

[10] T. Bu and L.B. Håøy. On the importance of correct inclusion of capillary pressure in reservoir simulation. Number 8 in IOR. European IOR - Symposium, 1995.

[11] G. Chavent and J. Jaffre. *Mathematical models and finite elements for reservoir simulation.* North-Holland, 1986.

[12] H.K. Dahle. *Adaptive Characteristic Operator Splitting Techniques for Convection-Dominated Diffusion Problems in One and Two Space Dimensions.* PhD thesis, University of Bergen, 1988. Department of Mathematics, University of Bergen.

[13] H.K. Dahle, M.S. Espedal, and O. Sævareid. Characteristic, local grid refinement techniques for reservoir flow problems. *International Journal for Numerical Methods in Engineering*, 34:1051–1069, 1992.

[14] J.Jr. Douglas and T.F. Russell. Numerical methods for convection-dominated diffusion problems based on combining the method of characteristics with finite element or finite difference procedures. *SIAM Journal on Numerical Analysis*, 19:871–885, 1982.

[15] K. Hvistendahl Karlsen, K. Brusdal, H. K. Dahle, S. Evje and K. A. Lie The Corrected Operator Splitting Approach Applied to Nonlinear Advection-Diffusion Problem, submitted to *Computer Methods in Applied Mechanics and Engineering.*

[16] T. Eilertsen, K.A. Børresen, H. Bertin, and A. Graue. Dimensional imaging experiments and numerical simulation of cross layered reservoir models. submitted to Journal of Petroleum Science and Engineering.

[17] M.S Espedal and R.E. Ewing. Characteristic petrov-galerkin subdomain methods for two-phase immiscible flow. *Computer Methods in Applied Mechanics and Engineering.*, 64:113–135, 1987.

[18] T. Gimse and N.H. Risebro. Solution of the cauchy problem for a conservation law with a discontinuous flux function. *SIAM Journal on Mathematical Analysis*, 23:635–648, 1992.

[19] T. Gimse and N.H. Risebro. A note on reservoir simulation for heterogeneous porous media. *Transport in Porous Media*, 10:257–270, 1993.

[20] A. Graue. Imaging the effects of capillary heterogeneities on local saturation development in long-core floods. Number 21101 in SPE. SPE Society of Petroleum Engineers, 1990.

[21] P.W. Hemker. *A numerical study of stiff two-point boundary problems.* PhD thesis, Mathematics Centrum, Amsterdam, 1977.

[22] J. Jaffre. Flux calculation at the interface between two rock types for two-phase flow in porous media. Technical Report 2075, INRIA, Domaine de Voluceau - Rocquencourt,le Chesnay,France, 1993.

[23] D.S. Koetsier. *Mechanisms affecting capillary entrapment in heterogeneous porous media.* PhD thesis, Delft University of Technology, 1993. Reservoir Engineering, Mining and Petroleum Engineering.

[24] B. G. Ersland and M. Espedal. *Domain Decomposition Method for Heterogeneous Reservoir Flow* Proceedings Eight International Conference on Domain Decomposition Methods, Beijing, China, May 16-20, 1995.

[25] H. K. Dahle, M. Espedal and X.-C. Tai. *A Characteristic Domain Splitting Method for Time-dependent Convection Diffusion Problems* Proceedings Eight International Conference on Domain Decomposition Methods, Beijing, China, May 16-20, 1995.

[26] T.F.M. Kortekaas. Water/oil displacement characteristics in crossbedded reservoir zones. *Society of Petroleum Engineers Journal*, pages 917–926, December 1985.

[27] J.I. Kristiansen, M. Mikkelsen, and K. Esbensen. A modified leverett approach and pls-regression for integrated formation evaluation. Number 33. Annual Symposium of Society of Professional Well Log Analysis, 1992.

[28] O. Sævareid. *On Local Grid Refinement Techniques for Reservoir Flow Problems.* PhD thesis, Department of Applied Mathematics, University of Bergen, 1990.

[29] K. W. Morton. *Numerical Solution of Convection-Diffusion Problems.* Applied Mathematics and Mathematical Computation 12, Chapman & Hall (1996).